Available online at www.sciencedirect.com
ScienceDirect
Trans. Nonferrous Met. Soc. China 35(2025) 945−953
Transactions of Nonferrous Metals Society of China
www.tnmsc.cn

3D inversion imaging of self-potential current source induced by mineral polarization

Li-juan ZHANG[1,2,3], Yi-an CUI[1,2,3], Jing XIE[4], Jian-xin LIU[1,2,3]

1. School of Geosciences and Info-physics, Central South University, Changsha 410083, China;
2. Hunan Key Laboratory of Nonferrous Resources and Geological Hazard Detection, Changsha 410083, China;
3. Key Laboratory of Metallogenic Prediction of Nonferrous Metals and Geological Environment Monitoring, Ministry of Education, Central South University, Changsha 410083, China;
4. School of Earth and Space Sciences, Peking University, Beijing 100871, China

Received 14 August 2023; accepted 13 May 2024

Abstract: An innovative gradient inversion approach employing the natural element method within the framework of least square regularization was proposed to enhance the quantitative interpretation of self-potential (SP) data originating from mineral polarization. The results indicated that the natural element method effectively addressed the challenge of subdividing complex resistivity models and aided in the accurate forward calculation of SP. By applying this approach to synthetic SP data and lab-measured SP data associated with redox electrochemical half-cell reactions of iron−copper metal blocks within the geobattery model, the 3D fine structure of buried orebody models was successfully reconstructed and the spatial distribution of SP current sources was mapped. This study significantly contributes to understanding the quantitative relationship between the polarization process of metal deposits and their corresponding SP responses and provides a valuable reference for delineating metal deposits in both terrestrial and marine environments through SP surveys.

Key words: mineral polarization; self-potential; natural element method; gradient inversion

1 Introduction

Metallic minerals are essential strategic materials for national economies, social development, and the defense industry. The imperative for mineral resources has been underscored by various international agreements such as the Paris Agreement on Climate Change and the 2030 Agenda for Sustainable Development [1]. As terrestrial mineral resources continue to be consumed at an increasing rate, the challenges and costs associated with exploration are also rising.

In contrast, the exploration and exploitation of marine mineral resources have emerged as a crucial foundation for sustainable development. The seafloor hosts a significant abundance of metallic mineral resources, including polymetallic nodules, cobalt-rich crusts, and polymetallic sulfides. Research into the exploration technology for seafloor hydrothermal polymetallic sulfides (SHPS) not only addresses the current exploration and development limitations of marine resources in China but also contributes to expanding national resource reserves, enhancing resource security, and advancing the development of marine power.

SHPS represent mineral deposits formed on the seafloor through the interaction of hot and metal-enriched fluids beneath the Earth's crust with cold seawater. These hydrothermal systems are typically

Corresponding author: Jing XIE, Tel: +86-18890090020, E-mail: jingpku@pku.edu.cn
DOI: https://doi.org/10.1016/S1003-6326(24)66725-7

associated with volcanic activity and are found in various locations, including mid-ocean ridges, back-arc basins, and other tectonic plate boundaries [2]. While there are approximately 1000 active submarine hydrothermal sites worldwide, as of 2020, only 390 SHPS zones or sites were identified [3].

SHPS deposits are significant reservoirs for essential base metals such as Cu, Zn, and Pb, as well as various other metals present in lower concentrations, including Ag, As, Au, Bi, Cd, Co, Ga, Ge, In, Hg, Mo, Ni, Re, Sb, Se, Sn, Te, and Tl [4]. These metals may exist as sulfides or occur as minor or trace elements within other sulfides and sulfosalts, making SHPS deposits potential sources for future mining operation. However, the exploration and extraction of SHPS deposits encounter various technical and environmental challenges due to their remote locations, extreme depths, and unique ecosystems.

Geophysical exploration technology plays a critical role in marine mineral exploration, providing a practical non-invasive approach for detecting inactive deposits in marine environments, particularly in the absence of geochemical plumes. Over recent decades, galvanometric and electro-magnetic methods have been extensively utilized for the exploration and assessment of SHPS resources. These methods encompass various techniques, including the electrical resistivity tomography [5], the transient electromagnetic method [6], the controlled source electromagnetic method [6,7], the self-potential (SP) method [8−12], as well as gravity and magnetic surveys [13]. The induced polarization method [14−16] is also an alternative technique.

Among the mentioned methods, the SP method exhibits a direct correlation with the natural polarization process observed in SHPS deposits. When an underground redox gradient is present, electrochemical half-cell reactions will occur around sulfide minerals, resulting in measurable negative SP anomalies near the seafloor. Moreover, SP surveys utilize simple equipment, comprising non-polarized electrodes and a sensitive voltmeter, making them suitable and cost-effective for large-scale exploration, offering high efficiency. An emerging solution involves installing electric field receivers on autonomous underwater vehicles for the SP measurements [8−10,17]. To carry out comprehensive investigations, SP surveys are often combined with other geophysical techniques, with the other methods primarily providing resistivity information [18−20].

In this work, a novel SP inversion scheme was proposed, which combined the natural element method (NEM) and the least square regularized gradient inversion algorithm (LSRGIA) to reconstruct the 3D distribution of SP current from SP data induced by mineral polarization. The primary objective of this study is to address the challenges associated with the subdivision of complex geoelectric models and the quantitative inversion of observed SP data.

2 Numerical method

2.1 SP boundary value problem

The Poisson equation governing conductivity and SP source density can be expressed as

$$\nabla \cdot \sigma \nabla u = \nabla \cdot \boldsymbol{j}_{\mathrm{SP}} \tag{1}$$

where σ is the local conductivity of media (S/m), u is the electric potential (V), and $\boldsymbol{j}_{\mathrm{SP}}$ is the SP source density (A/m^2).

In SP models, the current source exhibits characteristics of regional and multi-source distributions. The differential form of the current continuity equation can be written as

$$\nabla \cdot \boldsymbol{j}_{\mathrm{SP}} = -\sum_{i=1}^{N_I} I_i \delta(\boldsymbol{p} - \boldsymbol{p}_i) \tag{2}$$

where N_I is the number of power points, $\boldsymbol{p}$ means the check position, I_i is the current (A) at the active position $\boldsymbol{p}_i$, and δ represents the Dirac function and satisfies

$$\delta(\boldsymbol{p} - \boldsymbol{p}_i) = \begin{cases} 0, \ \boldsymbol{p} \neq \boldsymbol{p}_i \\ 1, \ \boldsymbol{p} = \boldsymbol{p}_i \end{cases} \tag{3}$$

Therefore, the SP Poisson equation can be rewritten as

$$\nabla \cdot \sigma \nabla u = -\sum_{i=1}^{N_I} I_i \delta(\boldsymbol{p} - \boldsymbol{p}_i) \tag{4}$$

At the surface boundary, the electric potential satisfies the Neumann boundary condition:

$$\frac{\partial u}{\partial \boldsymbol{n}} = 0 \tag{5}$$

At the truncated boundary, the mixed boundary condition with higher accuracy is often adopted:

$$\frac{\partial u}{\partial \boldsymbol{n}}+\frac{\cos(\boldsymbol{r},\boldsymbol{n})}{|\boldsymbol{r}|}u=0 \tag{6}$$

where $\boldsymbol{n}$ is the normal vector of the truncated boundary, and $\boldsymbol{r}$ means the radial vector from the power point to the truncated boundary. Equations (4)−(6) together form the boundary value problem of the SP field.

2.2 Natural element method

The commonly-used algorithms for solving SP boundary value problems include the finite element method (FEM) [21], finite difference method (FDM) [22], finite volume method (FVM) [23,24], finite-infinite element coupling method [25−28], and natural-infinite element coupling method [29,30]. However, the FEM, FDM, and FVM are limited by the requirement of mesh generation, while the coupling methods require additional computational efforts due to the incorporation of infinite elements. This study employed the 3D NEM with mixed boundary conditions, enabling precise subdivision of complex SP models and facilitating accurate forward calculations.

The NEM is an emerging meshless algorithm proposed by BRAUN and SAMBRIDGE [31]. It offers several advantages over traditional meshless and finite element methods in terms of computational efficiency and accuracy, such as higher accuracy in irregular domains and complex geometries, better stability and convergence for irregular or non-uniform distributions of nodes, flexibility in node layout, easy implementation, and reduced computational cost [30−34], and is well-suited for solving partial differential equations on highly irregular and evolving grids.

The NEM has three geometric elements: the Voronoi diagram, Delaunay tetrahedron partitioning, and natural neighbor interpolation. The natural neighbor interpolation encompasses Sibson interpolation and Laplace interpolation, with the latter exhibiting linear interpolation characteristics on both convex and concave boundaries. The construction and calculation of the shape function and its derivatives for 3D NEM based on Laplace interpolation are elucidated below.

As shown in Fig. 1 [30], assuming that the natural nodes are positioned at the vertices of the regular hexahedron, then: (1) the eight vertices serve as the natural neighbors of the interpolating point X within the hexahedron (see Fig. 1(a)); (2) utilizing the 9-node discrete points, a Delaunay tetrahedral grid system can be established (see Fig. 1(a)); (3) spheres circumscribing these tetrahedrons are drawn, allowing the determination of the coordinates of the corresponding sphere centers (see Fig. 1(b)); (4) all these sphere centers collectively constitute the second-order Voronoi convex polyhedron of the interpolating point X (see Fig. 1(c)).

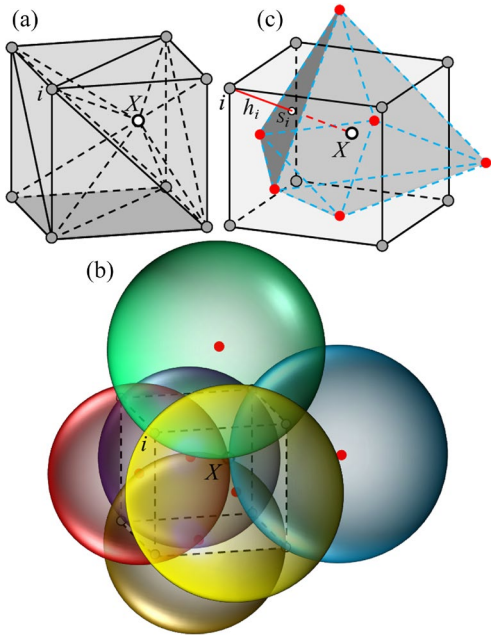

Fig. 1 Geometric elements of 3D NEM: (a) Delaunay tetrahedrons of 9-node system; (b) Delaunay circumscribed spheres and their centers; (c) Second-order Voronoi convex polyhedron of point X formed through these centers (Redraw from [30])

The shape function for each natural neighbor corresponding to the point X can be expressed as

$$N_i(x,y,z)=\frac{\alpha_i(x,y,z)}{\sum_{j=1}^{n}\alpha_j(x,y,z)} \tag{7}$$

where $\alpha_i(x,y,z)=S_i(x,y,z)/h_i(x,y,z)$, $S_i(x, y, z)$ means the area of the second-order Voronoi surface associated with the natural neighbor i, $h_i(x, y, z)$ represents half of the distance from the point X to the natural neighbor i, and n is the number of natural neighbors. The partial derivative of the shape function with respect to coordinates can be expressed as

$$N_{i,\mathfrak{R}}(x,y,z)=\frac{\alpha_{i,\mathfrak{R}}(x,y,z)-N_i(x,y,z)\sum_{j=1}^{n}\alpha_{j,\mathfrak{R}}(x,y,z)}{\sum_{j=1}^{n}\alpha_j(x,y,z)} \tag{8}$$

where $\mathfrak{R}$ represents the coordinates x, y, and z.

2.3 Least square regularized gradient inversion

SP inversion is a well-known ill-posed problem, characterized by a non-unique solution. It is therefore important to introduce additional constraints to reduce the solution space. The criteria of data misfit and model objective function place different and competing requirements on the SP models [35]. Typically, Tikhonov regularization [36] is employed to balance the two objective functions. The LSRGIA used in this study was originally proposed and developed by ZHU et al [11], GUO et al [20], JARDANI et al [35,37], MARTÍNEZ-PAGÁN et al [38], and MAO et al [39].

The primary requirement for inversion is to ensure consistency between the predicted and observed SP data, which can be evaluated using the data misfit function C_d:

$$C_d=||\boldsymbol{W}_d(\boldsymbol{K}^{-1}\boldsymbol{m}-\boldsymbol{d}_{obs})|| \tag{9}$$

where $||\boldsymbol{v}||$ represents the Euclidean norm, $\boldsymbol{W}_d$ is the square diagonal weighting matrix, $\boldsymbol{m}$ means a vector illustrating the SP current, $\boldsymbol{K}^{-1}$ is the inverse of the stiffness matrix $\boldsymbol{K}$, $\boldsymbol{K}^{-1}\boldsymbol{m}$ is the predicted SP responses, and $\boldsymbol{d}_{obs}$ is the observed SP data. If the number of observation points and model nodes is N and M, respectively (usually $N \ll M$), then the dimensions of $\boldsymbol{W}_d$, $\boldsymbol{K}^{-1}$, $\boldsymbol{m}$, and $\boldsymbol{d}_{obs}$ are $N\times N$, $N\times M$, $M\times 1$, and $N\times 1$, respectively.

To better constrain the solution space, the model that most likely represents the true distribution of underground SP sources can be obtained by evaluating the structural complexity of the model, in which the distribution of underground conductivity constrains that of SP sources, making the imaging of underground abnormal bodies more consistent with true models. The corresponding objective function C_m can be expressed as

$$C_m=||\boldsymbol{W}_m(\boldsymbol{m}-\boldsymbol{m}_{ref})|| \tag{10}$$

where $\boldsymbol{W}_m$ is the weighting matrix with a dimension of $M\times M$, and $\boldsymbol{m}_{ref}$ is a reference model.

The optimal model is achieved by minimizing the model objective function C_m while simultaneously fitting the data objective function C_d within a predetermined threshold. The competing roles of data misfit and model objective function are balanced using Tikhonov regularization through a global objective function (ψ):

$$\psi(\boldsymbol{m})=||\boldsymbol{W}_d(\boldsymbol{K}^{-1}\boldsymbol{m}-\boldsymbol{d}_{obs})||^2+\lambda||\boldsymbol{W}_m(\boldsymbol{m}-\boldsymbol{m}_{ref})||^2 \tag{11}$$

where $||\boldsymbol{v}||^2=(\boldsymbol{v}^T\boldsymbol{v})$, and λ is a regularization parameter.

Expand Eq. (11) to get

$$\begin{aligned}\psi(\boldsymbol{m})=&[\boldsymbol{W}_d(\boldsymbol{K}^{-1}\boldsymbol{m}-\boldsymbol{d}_{obs})]^T[\boldsymbol{W}_d(\boldsymbol{K}^{-1}\boldsymbol{m}-\boldsymbol{d}_{obs})]+\\ &\lambda[\boldsymbol{W}_m(\boldsymbol{m}-\boldsymbol{m}_{ref})]^T[\boldsymbol{W}_m(\boldsymbol{m}-\boldsymbol{m}_{ref})]=\\ &(\boldsymbol{K}^{-1}\boldsymbol{m}-\boldsymbol{d}_{obs})^T\boldsymbol{W}_d^T\boldsymbol{W}_d(\boldsymbol{K}^{-1}\boldsymbol{m}-\boldsymbol{d}_{obs})+\\ &\lambda(\boldsymbol{m}-\boldsymbol{m}_{ref})^T\boldsymbol{W}_m^T\boldsymbol{W}_m(\boldsymbol{m}-\boldsymbol{m}_{ref})\end{aligned} \tag{12}$$

The minimum solution of the global objective function ψ can be obtained by taking the derivative of ψ with respect to $\boldsymbol{m}$ and setting it to zero [40]:

$$\begin{aligned}\boldsymbol{m}=&[(\boldsymbol{K}^{-1})^T\boldsymbol{W}_d^T\boldsymbol{W}_d(\boldsymbol{K}^{-1})+\lambda\boldsymbol{W}_m^T\boldsymbol{W}_m]^{-1}\cdot\\ &[(\boldsymbol{K}^{-1})^T\boldsymbol{W}_d^T\boldsymbol{W}_d\boldsymbol{d}_{obs}+\lambda\boldsymbol{W}_m^T\boldsymbol{W}_m\boldsymbol{m}_{ref}]\end{aligned} \tag{13}$$

In addition, based on the weighting matrix $\boldsymbol{W}_m$ proposed by MINSLEY et al [41], $\boldsymbol{W}_m$ can be defined as

$$(\boldsymbol{W}_m)_{j=1\to M}=\mathrm{diag}\left(\sqrt[4]{\sum_{i=1}^{M}(\boldsymbol{K}_{ij}^{-1})^2}\right) \tag{14}$$

3 Inversion example

In this section, we assessed the efficacy of SP data in reconstructing SP current through both a synthetic model and lab-measured data. The lab-scale experiment focused on real-time monitoring of anodizing corrosion of metallic sphere and cylinder model.

3.1 Synthetic model

The synthetic two-layer model had dimensions of 400 m × 200 m × 150 m ($X\times Y\times Z$). The upper layer was 20 m in thickness, with resistivity values of 200 and 400 Ω·m for the upper and lower layers, respectively. Two low-resistance conductive ore bodies were present within the model, each measuring 40 m × 40 m × 40 m and having a resistivity value of 1 Ω·m. Their respective center coordinates were (−100 m, 0 m, −40 m) and (100 m, 0 m, −60 m), with the origin of the Cartesian coordinate system located at the center of the model surface.

During the forward modeling step, the SP current within the ore body regions was set to be −1 mA at discrete model points. The iterative method employed to solve the linear equations is the biconjugate gradient stabilized method based on incomplete LU decomposition.

During the inversion process, the threshold for the global objective function ψ was set to be 10. The initial regularization parameter λ was 0.1 and decreased by 80% after each subsequent iteration. Since both the measured data and prior model information were assumed to be unknown, the data weighting matrix $\boldsymbol{W}_{\mathrm{d}}$ was defined as the identity matrix, and the prior model $\boldsymbol{m}_{\mathrm{ref}}$ was set as the zero matrix. The initial current was −0.001 mA, and the measurement points were spaced at intervals of 10 m, with the corresponding forward data used for the inversion input.

Figure 2 illustrates the variation of the global objective function ψ with iteration number, demonstrating that higher levels of noise lead to an increased number of iterations. The values of ψ obtained at the final iteration were 9.35, 6.74, and 7.82 for 0%, 5%, and 10% noise, respectively. As the contribution of the model objective function gradually diminishes to zero during the iterative process, the last ψ primarily reflects the fitness between the predicted and observed data.

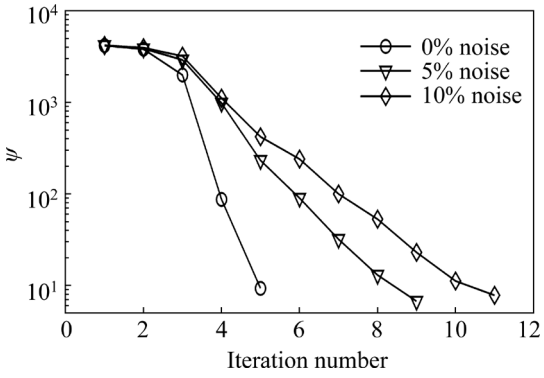

Fig. 2 Variation of global objective function ψ with iteration number

Figure 3 depicts the inversion results of the SP current for noise levels of 0%, 5%, and 10%, respectively. Only negative SP currents with amplitudes exceeding 0.01 mA were displayed, and the true SP source distribution was outlined by black hexahedron boxes. It is observed that: (1) in the absence of noise, the 3D NEM-based LSRIGA successfully reconstructs the true distribution of SP sources (see Fig. 3(a)); (2) with increasing noise levels, the contours of the recovered ore bodies gradually become distorted (refer to Figs. 3(b) and (c)); (3) the inversion results obtained from noisy SP data generate false anomalies on the surface, and the magnitude of these anomalies increases with the increase of the noise level. However, despite these distortions, the reconstructed SP source distribution still approximates the true ones and exhibits some overlap. These findings demonstrate that the LSRIGA, incorporating both data misfit and model constraints, is capable of reconstructing the 3D structure of subsurface mineral deposits.

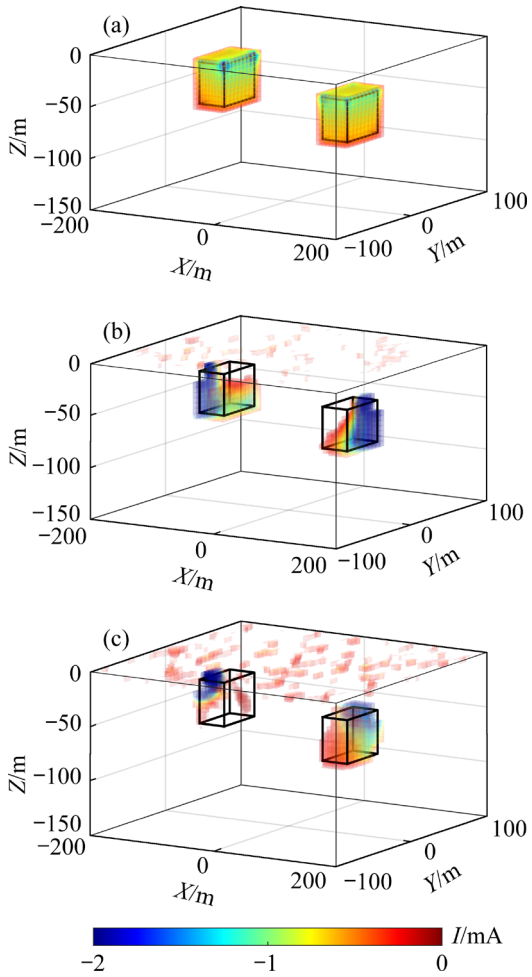

Fig. 3 Recovered SP current obtained from forward SP data of synthetic model, with noise levels of 0% (a), 5% (b), and 10% (c)

3.2 Lab-measured SP data

3.2.1 Vertical polarization of spherical model

The primary objective of the lab-based redox monitoring experiment is to observe the natural polarization process, which involves the electron transfer mechanism and electrochemical half-cell

reactions involving the oxidation of iron (Fe) and the reduction of oxygen (O_2). The experimental platform employed in this study offers automation, real-time monitoring, stability, and sensitivity. It is capable of conducting various types of SP generation and observation experiments, including naturally polarized redox SP signals mediated by ore bodies, redox SP signals related to the degradation of organic matter mediated by bacteria, and streaming potential signals caused by the electrokinetic effect of fluid flow. More detailed information regarding the experimental setup, procedure, and redox theory can be found in Ref. [42].

Figure 4 illustrates the configurations employed in the vertical polarization monitoring experiment, and Fig. 5 provides a sketch of the setup. It is evident that the initial sphere model is pristine, but after the redox experiment, Fe(III)-related rust accumulates on the iron hemisphere, while the copper hemisphere remains unaffected due to its role in electron transfer downward to oxygen (O_2, the electron acceptor).

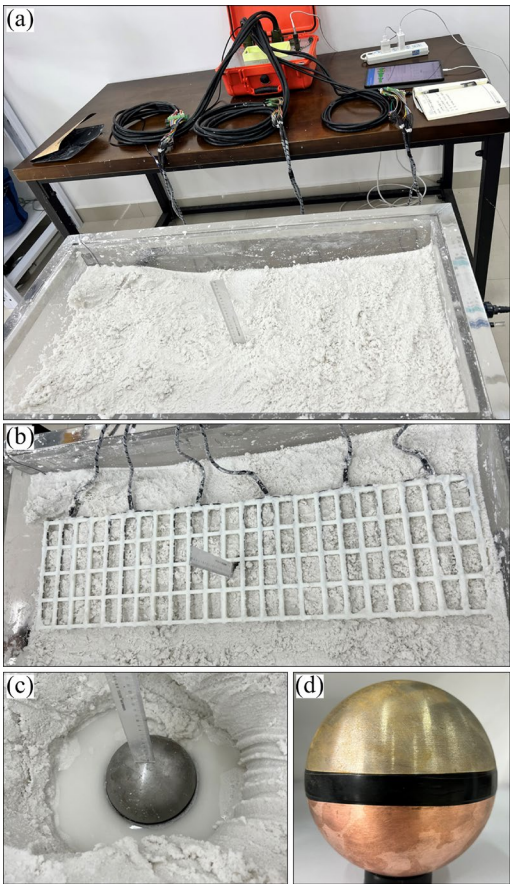

Fig. 4 Configurations of lab-scale redox monitoring experiment: (a) Complete experimental setup; (b) 120-channel non-polarized Ag/AgCl electrode shelf; (c) Iron−copper sphere measuring 15 cm in diameter, positioned across water table; (d) Fe(III)-related rust on iron hemisphere after redox experiment

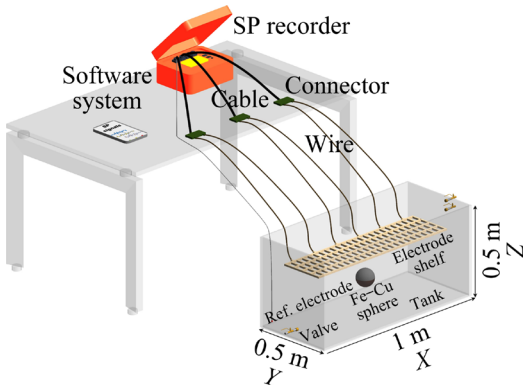

Fig. 5 Sketch of experimental setup

In this experiment, the smooth metal sphere and the artificially created redox interface (iron−copper interface) facilitate rapid redox electrochemical half-cell reactions, leading to the generation of strong, pure, and high-quality SP data. Figure 6 represents the contour map of the 120-channel SP data measured at the 450th record. The SP distribution exhibits a symmetrical characteristic about both the *X*- and *Y*-axes, and decays in concentric circles with increasing distance. The measured SP data were quantitatively interpreted using the proposed inversion algorithm.

For the inversion, the lab-scale model had dimensions of 1 m × 0.5 m × 0.4 m. The upper wet layer, located above the water table, had a thickness of 17.5 cm and a resistivity of approximately 150 Ω·m. The lower layer was fully saturated with a resistivity of around 100 Ω·m. The resistivity values for the iron and copper hemispheres are 9.78×10^{-8} and 1.75×10^{-8} Ω·m, respectively. However, to avoid numerical singularity during the inversion, the resistivity of the sphere was set to be 0.1 Ω·m.

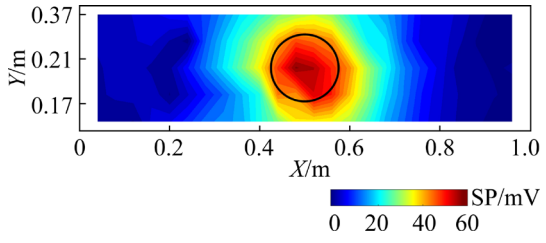

Fig. 6 Contour map of 120-channel SP data measured at the 450th record, with black circle representing horizontal projection position of sphere

The inversion results are presented in Fig. 7, revealing the following observations: (1) the distribution of SP sources is well-aligned with the spherical model; (2) the gradient inversion of SP data effectively determines the depth and shape of the buried low-resistance object; (3) the surface noise does not impact the characterization of the buried target.

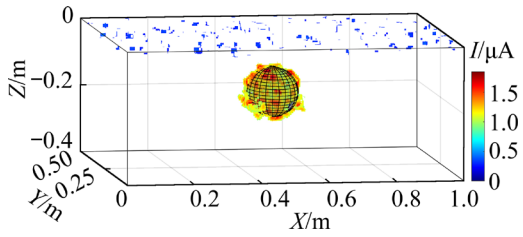

Fig. 7 Estimated SP current from measured SP data of vertically polarized sphere (Transparent sphere represents real position of iron−copper sphere)

3.2.2 Vertical polarization of cylindrical model

Conducting redox experiments with various polarization blocks provides valuable insight into the macroscopic SP anomalies of the geobattery model and facilitates the exploration of SP identifications associated with different polarization characteristics. In addition to the vertical polarization monitoring experiment of the spherical model, the vertical polarization process of a cylindrical metal block was also concerned. Figure 8 shows the configurations employed in the experiment and the changes of Fe(III)-related rust covered on the iron cylinder.

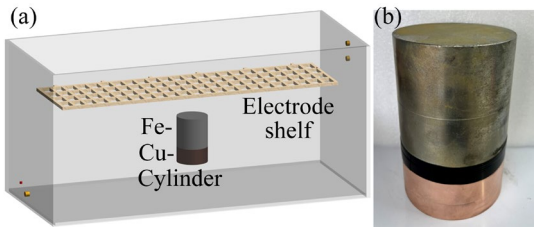

Fig. 8 Configurations in tank with cylinder being 10 cm in diameter and 15 cm in length (iron part is 10 cm in length and copper part is 5 cm in length) (a), and Fe(III)-related rust on iron cylinder after redox experiment (b)

The 3D inversion imaging was conducted using the 120-channel SP data measured at the 450th record. The inversion results, as depicted in Fig. 9, demonstrate a close match between the distribution of SP sources and the cylindrical model, providing further validation of the accuracy and resolution of the proposed inversion imaging algorithm.

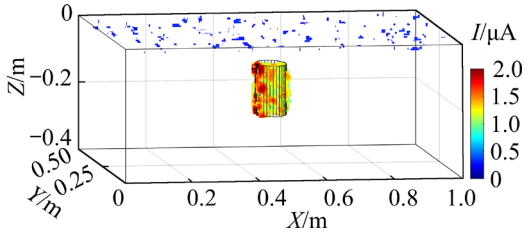

Fig. 9 Estimated SP current from measured SP data of vertically polarized cylinder (Transparent cylinder represents real position of iron−copper cylinder)

4 Conclusions

(1) The utilization of the meshless NEM effectively addresses the boundary value problem associated with SP models, enabling the subdivision of complex geometric structures through flexible node filling.

(2) The inversion examples of synthetic and lab-measured SP data prove that the proposed 3D NEM-based LSRIGA, incorporating both data misfit and model constraints, can accurately reconstruct the 3D distribution of SP current.

(3) The inversion results highlight the potential of SP surveys as a promising tool for locating buried metal blocks, and this study holds significant relevance for the application of SP surveys in the exploration and development of marine mineral resources.

CRediT authorship contribution statement

Li-juan ZHANG: Conceptualization, Investigation, Methodology, Visualization, Writing − Review & editing; **Yi-an CUI:** Conceptualization, Funding acquisition, Supervision; **Jing XIE:** Conceptualization, Methodology, Software, Visualization, Writing − Original draft, Review & editing; **Jian-xin LIU:** Supervision.

Declaration of competing interest

The authors declare that they have no known competing financial interests or personal relationships that could have appeared to influence the work reported in this paper.

Acknowledgments

This work was supported by the National Natural Science Foundation of China (No. 42174170).

References

[1] LIU Y, LI J B, WANG Y J, TAO C H, ZENG Z G, HAN X Q, LI C S, ZHOU Y D, LIANG J. Development and prospect of exploration and research on seafloor polymetallic sulfides of China [J]. The Chinese Journal of Nonferrous Metals, 2021, 31(10): 2624−2637. (in Chinese)

[2] HOAGLAND P, BEAULIEU S, TIVEY M A, EGGERT R G, GERMAN C, GLOWKA L, LIN J. Deep-sea mining of seafloor massive sulfides [J]. Marine Policy, 2010, 34: 728−732.

[3] BEAULIEU S E, SZAFRAŃSKI K M. InterRidge global database of active submarine hydrothermal vent fields version 3.4 [DB/OL]. Paris: Institute de Plysique du Globe de Paris, 2020. https://doi.org/10.1594/PANGAEA.917894.

[4] FONTBOTÉ L, KOUZMANOV K, CHIARADIA M, POKROVSKI G S. Sulfide minerals in hydrothermal deposits [J]. Elements, 2017, 13(2): 97−103.

[5] ISHIZU K, GOTO T, OHTA Y, KASAYA T, IWAMOTO H, VACHIRATIENCHAI C, SIRIPUNVARAPORN W, TSUJI T, KUMAGAI H, KOIKE K. Internal structure of a seafloor massive sulfide deposit by electrical resistivity tomography, Okinawa Trough [J]. Geophysical Research Letters, 2019, 46(20): 11025−11034.

[6] HAROON A, HÖLZ S, GEHRMANN R A S, ATTIAS E, JEGEN M, MINSHULL T A, MURTON B J. Marine dipole−dipole controlled source electromagnetic and coincident-loop transient electromagnetic experiments to detect seafloor massive sulphides: Effects of three-dimensional bathymetry [J]. Geophysical Journal International, 2018, 215(3): 2156−2171.

[7] GEHRMANN R A S, NORTH L J, GRABER S, SZITKAR F, PETERSEN S, MINSHULL T A, MURTON B J. Marine mineral exploration with controlled source electromagnetics at the TAG hydrothermal field, 26°N Mid Atlantic Ridge [J]. Geophysical Research Letters, 2019, 46(11): 5808−5816.

[8] CONSTABLE S, KOWALCZYK P, BLOOMER S. Measuring marine self-potential using an autonomous underwater vehicle [J]. Geophysical Journal International, 2018, 215(1): 49−60.

[9] KAWADA Y, KASAYA T. Self-potential mapping using an autonomous underwater vehicle for the Sunrise deposit, Izu-Ogasawara arc, Southern Japan [J]. Earth, Planets and Space, 2018, 70(1): 142.

[10] SU Z Y, TAO C H, SHEN J S, REVIL A, ZHU Z M, DENG X M, NIE Z F, LI Q Y, LIU L, WU T, ZHOU J P, CHEN D. 3D self-potential tomography of seafloor massive sulfide deposits using an autonomous underwater vehicle [J]. Geophysics, 2022, 87(4): B255−B267.

[11] ZHU Z M, TAO C H, SHEN J S, REVIL A, DENG X M, LIAO S, ZHOU J P, WANG W Y, NIE Z F, YU J. Self-potential tomography of a deep-sea polymetallic sulfide deposit on Southwest Indian Ridge [J]. Journal of Geophysical Research: Solid Earth, 2020, 125(11): e2020JB019738.

[12] XIE J, CUI Y A, LIU J X, GUO Y J, ZHANG L J, LUO Y J, ZHANG P F. A review on theory, modeling, inversion, and application of self-potential in marine mineral exploration [J]. Transactions of Nonferrous Metals Society of China, 2023, 33(4): 1214−1232.

[13] GALLEY C, LELIÈVRE P, HAROON A, GRABER S, JAMIESON J, SZITKAR F, YEO I, FARQUHARSON C, PETERSEN S, EVANS R. Magnetic and gravity surface geometry inverse modeling of the TAG active mound [J]. Journal of Geophysical Research: Solid Earth, 2021, 126(10): e2021JB022228.

[14] HAN S L, ZHANG S G, LIU J X, HU H J, ZHANG W S. Integrated interpretation of dual frequency induced polarization measurement based on wavelet analysis and metal factor methods [J]. Transactions of Nonferrous Metals Society of China, 2013, 23(5): 1465−1471.

[15] LIU H F, LIU J X, GUO R W, TONG X Z, GONG L, PENG Y H. Development of multi-channel observation and inversion for IP electrical sounding method [J]. Transactions of Nonferrous Metals Society of China, 2014, 24(3): 816−823.

[16] REVIL A, VAUDELET P, SU Z Y, CHEN R J. Induced polarization as a tool to assess mineral deposits: A review [J]. Minerals, 2022, 12(5): 571.

[17] ZHU Z M, SHEN J S, TAO C H, DENG X M, WU T, NIE Z F, WANG W Y, SU Z Y. Autonomous-underwater-vehicle-based marine multicomponent self-potential method: Observation scheme and navigational correction [J]. Geoscientific Instrumentation, Methods and Data Systems, 2021, 10: 35−43.

[18] SU Z Y, TAO C H, ZHU Z M, REVIL A, SHEN J S, NIE Z F, LI Q Y, DENG X M, ZHOU J P, LIU L. Joint interpretation of marine self-potential and transient electromagnetic survey for seafloor massive sulfide (SMS) deposits: Application at TAG hydrothermal mound, Mid-Atlantic Ridge [J]. Journal of Geophysical Research: Solid Earth, 2022, 127: e2022JB024496.

[19] KASAYA T, IWAMOTO H, KAWADA Y, HYAKUDOME T. Marine DC resistivity and self-potential survey in the hydrothermal deposit areas using multiple AUVs and ASV [J]. Terrestrial, Atmospheric and Oceanic Sciences, 2020, 31(5): 579−588.

[20] GUO Y J, CUI Y A, XIE J, LUO Y J, ZHANG P F, LIU H F, LIU J X. Seepage detection in earth-filled dam from self-potential and electrical resistivity tomography [J]. Engineering Geology, 2022, 306: 106750.

[21] SOUEID AHMED A, JARDANI A, REVIL A, DUPONT J P. SP2DINV: A 2D forward and inverse code for streaming potential problems [J]. Computers & Geosciences, 2013, 59: 9−16.

[22] MENDONÇA C A. Forward and inverse self-potential modeling in mineral exploration [J]. Geophysics, 2008, 73(1): F33−F43.

[23] XIE J, CUI Y A, NIU Q F. Coupled inversion of hydraulic and self-potential data from transient outflow experiments to estimate soil petrophysical properties [J]. Vadose Zone Journal, 2021, 20(5): e20157.

[24] BIENVENUE T, XIE J, NIU Q F. Developing a soil column system to measure hydrogeophysical properties of unconsolidated sediment [J]. Vadose Zone Journal, 2022,

21(2): e20186.
[25] XIE J, CUI Y A, ZHANG L J, MA C Y, YANG B, CHEN X L, LIU J X. 3D forward modeling of seepage self-potential using finite-infinite element coupling method [J]. Journal of Environmental and Engineering Geophysics, 2020, 25(3): 381−390.
[26] XIE J, CUI Y A, ZHANG L J, GUO Y J, WANG J X, FANIDI M, LIU J X. Numerical modeling of biogeobattery system from microbial degradation of underground organic contaminant [J]. SN Applied Sciences, 2020, 2: 208.
[27] XIE J, CUI Y A, FANIDI M, ZHANG L J, GUO Y J, LUO Y J, LIU J X. Numerical modeling of marine self-potential from a seafloor hydrothermal ore deposit [J]. Pure and Applied Geophysics, 2021, 178: 1731−1744.
[28] XIE J, DU X Z, CUI Y A, LUO Y J, ZHANG L J, GUO Y J, LIU J X. Numerical modeling for 4-D self-potential resistivity model [J]. Pure and Applied Geophysics, 2023, 180: 205−213.
[29] XIE J, CUI Y A, GUO Y J, ZHANG L J, FANIDI M, LIU J X. 2.5D self-potential forward modeling by natural-infinite element coupling method [J]. Journal of Applied Geophysics, 2020, 179: 104077.
[30] XIE J, CUI Y A, CHEN H, LUO Y J, GUO Y J, LIU J X. 3D DC resistivity numerical modeling by natural-infinite element coupling method [J]. Chinese Journal of Geophysics, 2023, 66(6): 2670−2684. (in Chinese)
[31] BRAUN J, SAMBRIDGE M. A numerical method for solving partial differential equations on highly irregular evolving grids [J]. Nature, 1995, 376(6542): 655−660.
[32] CHEN J S, PAN C. Natural element method: In encyclopedia of computational mechanics [M]. New York: John Wiley & Sons, Ltd., 2015.
[33] LIU W K, JUN S, ZHANG Y F. Reproducing kernel particle methods [J]. International Journal for Numerical Methods in Fluids, 1995, 20(8/9): 1081−1106.
[34] REN H, CHEN J S. Natural element method for computational mechanics [J]. Computational Mechanics, 2005, 36(5): 383−396.
[35] JARDANI A, REVIL A, BOLÈVE A, CRESPY A, DUPONT J P, BARRASH W, MALAMA B. Tomography of the Darcy velocity from self-potential measurements [J]. Geophysical Research Letters, 2007, 34: L24403.
[36] TIKHONOV A N, ARSENIN V Y. Solutions of ill-posed problems [M]. Hoboken, USA: John Wiley, 1977.
[37] JARDANI A, REVIL A, BOLÈVE A, DUPONT J P. Three-dimensional inversion of self-potential data used to constrain the pattern of groundwater flow in geothermal fields [J]. Journal of Geophysical Research: Solid Earth, 2008, 113: B09204.
[38] MARTÍNEZ-PAGÁN P, JARDANI A, REVIL A, HAAS A. Self-potential monitoring of a salt plume [J]. Geophysics, 2010, 75(4): 17−25.
[39] MAO D Q, REVIL A, HORT R D, MUNAKATA-MARR J, ATEKWANA E A, KULESSA B. Resistivity and self-potential tomography applied to groundwater remediation and contaminant plumes: Sandbox and field experiments [J]. Journal of Hydrology, 2015, 530: 1−14.
[40] HANSEN P C. Rank-deficient and discrete ill-posed problems: Numerical aspects of linear inversion [M]. Philadelphia, USA: Soc. for Industrial and Applied Mathematics, 1998.
[41] MINSLEY B J, SOGADE J, MORGAN F D. Three-dimensional source inversion of self-potential data [J]. Journal of Geophysical Research: Solid Earth, 2007, 112: B02202.
[42] XIE J, CUI Y A, ZHANG L J, GUO Y J, CHEN H, ZHANG P F, LIU J X. Redox mechanism of geobattery and related electrical signals using a novel real-time self-potential monitoring experimental platform [J]. Journal of Central South University, 2024, 31(11): 4155−4173.

矿体极化自然电位电流源三维反演成像

张丽娟[1,2,3]，崔益安[1,2,3]，谢 静[4]，柳建新[1,2,3]

1. 中南大学 地球科学与信息物理学院，长沙 410083；
2. 有色资源与地质灾害探查湖南省重点实验室，长沙 410083；
3. 中南大学 有色金属成矿预测与地质环境监测教育部重点实验室，长沙 410083；
4. 北京大学 地球与空间科学学院，北京 100871

摘 要：提出一种基于自然单元法的最小二乘正则化自然电位精细梯度反演方法以提高矿物极化自然电位数据的定量解释效果。结果表明，自然单元法有效解决了复杂电阻率模型的剖分问题，便于开展自然电位精细正演计算。通过将该梯度反演算法应用于合成数据以及铁铜金属块氧化还原监测实验测量数据，成功重构了埋藏矿体模型的三维精细结构，并绘制了自然电位电流源的空间分布图。本研究有助于了解金属矿床极化过程与其自然电位响应之间的定量关系，为自然电位法圈定陆地及海底金属矿床提供有益参考。

关键词：矿物极化；自然电位；自然单元法；梯度反演

(Edited by Wei-ping CHEN)